Shape of a tethered filament in various low-Reynolds-number flows

Christina Kurzthaler [1,2,*] Rodolfo Brandão [2,3] Ory Schnitzer [3,†] and Howard A. Stone [2,‡]

[1] *Max Planck Institute for the Physics of Complex Systems, 01187 Dresden, Germany*
[2] *Department of Mechanical and Aerospace Engineering,*
Princeton University, Princeton, New Jersey 08544, USA
[3] *Department of Mathematics, Imperial College London, London SW7 2AZ, United Kingdom*

We consider the steady-state deformation of an elastic filament in various unidirectional, low-Reynolds-number flows, with the filament either clamped at one end, perpendicular to the flow, or tethered at its center and deforming symmetrically about a plane parallel to the flow. We employ a slender-body model [Pozrikidis, J. Fluids Struct. **26**, 393 (2010)] to describe the filament shape as a function of the background flow and a nondimensional compliance η characterizing the ratio of viscous to elastic forces. For $\eta \ll 1$, we describe the small deformation of the filament by means of a regular perturbation expansion. For $\eta \gg 1$, the filament strongly bends such that it is nearly parallel to the flow except close to the tether point; we analyze this singular limit using boundary-layer theory, finding that the radius of curvature near the tether point, as well as the distance of the parallel segment from the tether point, scale like $\eta^{-1/2}$ for flow profiles that do not vanish at the tether point, and like $\eta^{-1/3}$ for flow profiles that vanish linearly away from the tether point. We also use a Wentzel-Kramers-Brillouin approach to derive a leading-order approximation for the exponentially small slope of the filament away from the tether point. We compare numerical solutions of the model over a wide range of η values with closed-form predictions obtained in both asymptotic limits, focusing on particular uniform, shear and parabolic flow profiles relevant to experiments.

I. INTRODUCTION

Hydrodynamic couplings of filaments with flows are a fundamental aspect of the functioning of various biological and synthetic systems. The latter include the self-propulsion of microorganisms via the beating of individual flagella [1], the cooperative beating of cilia in airways to transport mucus [2], the generation of feeding flows by cilia attached to the surface of corals [3], the rotation of cilia for the development of the left-right asymmetry during embryogenesis [4–7], and the use of artificial filaments for stirring fluid flows at the microscale [8–10]. In these distinct systems, the filaments are typically tethered to a surface and the interplay of complex molecular processes and

*ckurzthaler@pks.mpg.de
†o.schnitzer@imperial.ac.uk
‡hastone@princeton.edu

intricate interactions with their neighbors dictate the dynamics [11]. In addition, filaments can be found in the interior of cells, such as DNA strands and cytoskeletal polymers, where, while being subject to strong confinement and hydrodynamic flows, they drive cellular processes, such as mitosis and migration [12,13].

Experimental studies have shown that attachment of slender bodies, such as DNA strands [14,15], cilia [16], and bacterial pili [17], to surfaces can provide insights into their dynamical features, such as the extension and retraction cycle of pili via binding of specific motor proteins [17], and allow for quantitative measurement of their elastic properties via the application of external flows. To infer material properties of these small-scale systems, theoretical predictions for their geometric properties in flows are required.

Theoretical studies, building on the seminal work on slender-body theories of Cox [18], Batchelor [19], Lighthill [20], Keller and Rubinow [21], and Johnson [22], as well as the classical bead-spring model [23–25], have addressed the behavior of individual filaments in flow and the predictions for the filament motion and shape have also been successfully compared to experimental observations. A large aspect of recent research concerns the motion of filaments in different microscale flows, which exhibit interesting dynamics ranging from tumbling motion [26] to buckling phenomena [27–33]. In addition, the dynamics of sedimenting fibers have been studied extensively [34–36] and experimentally measured scaling behaviors of the deformation of flexible fibers have been compared to a slender-body theory at small deformation and a bead–spring model at large deformation [36].

For the case of tethered filaments, the extension of DNA molecules in uniform flow [15], the deformation of a tethered fiber in confinement [37], the buckling behavior in a stagnation flow [38], and the physics of a rotating filament have been elucidated [39,40]. In addition, Brownian effects on the dynamics of tethered filaments have been studied in an oscillatory flow [41] and in shear flow [42,43], where scaling relations are provided at strong driving [43]. However, perhaps surprisingly, theoretical predictions and scalings for the deformation of a single tethered filament in simple flows have not been provided so far, even in the absence of Brownian forces.

Here, we consider the steady-state deformation of a tethered elastic filament in various unidirectional, low-Reynolds-number flows. We shall adopt a general formulation where the filament is either clamped at one end, in a direction perpendicular to the flow, or tethered at its center, deforming symmetrically about a plane that is parallel to the flow and passes through its center. This will allow us to focus on several experimentally relevant scenarios, including a filament clamped to a wall in simple shear flow and a centrally tethered filament in uniform and parabolic-channel flows. An important nondimensional number in this system represents the compliance, which measures the viscous forces with respect to the elastic forces acting on the filament. For small compliances, where elastic forces dominate over viscous forces, we expect that the tethered filament only displays a small deflection from its nominal straight configuration perpendicular to the flow. In contrast, at large compliances one expects that the filament is strongly bent, such that it is essentially aligned with the flow except close to the tether point. Using the model proposed by Pozrikidis in Ref. [44], we shall theoretically characterize this transition as a function of the compliance and develop analytical predictions for small and large compliances, respectively. As further discussed later in this paper, we shall rely in this study on a local slender-body description, which neglects the disturbance flows produced by the filament and, consequently, hydrodynamic coupling of the filament with itself and nearby walls.

II. PROBLEM FORMULATION

A. Slender-body model

Consider a slender filament tethered at the origin of a Cartesian coordinate system (x^*, y^*, z^*). (An asterisk indicates a dimensional quantity.) The filament is immersed in a fluid of viscosity μ^*, which may either be infinite or confined by physical boundaries parallel to the x^* axis. We wish to model the steady-state deformation, in the $x^* - y^*$ plane, of the filament as a result of an ambient
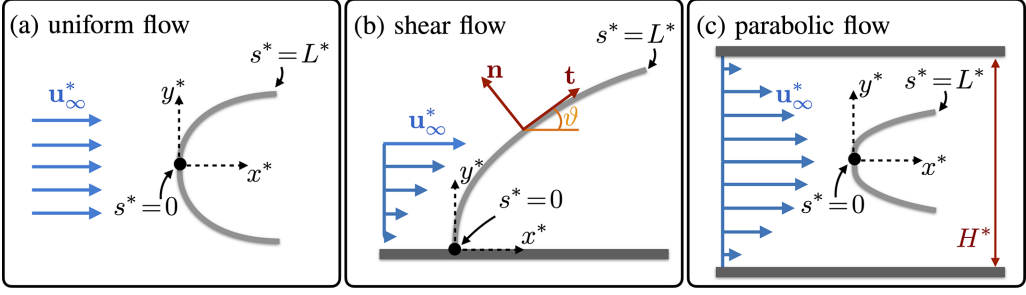
FIG. 1. Tethered filament deforming in a unidirectional flow $\mathbf{u}_\infty^*$: (a) filament of length $2L^*$, tethered at its center, in a uniform flow; (b) filament of length L^*, perpendicularly clamped to a wall in simple shear flow; and (c) filament of length $2L^*$, tethered at its center, in a parabolic channel flow. The flow profiles $\mathbf{u}_\infty^*$ are defined in Table I.

perpendicular flow,

$$\mathbf{u}_\infty^* = u^*(y^*)\hat{\mathbf{e}}_x, \tag{1}$$

where $\hat{\mathbf{e}}_x$ is a unit vector in the x^* direction and $u^*(y^*)$ is a unidirectional flow profile. The latter satisfies $\mu^* d^2 u^*/dy^{*2} = dp^*/dx^*$, where dp^*/dx^* is a possible pressure gradient, as well as hydrodynamic boundary conditions at the physical boundaries. The filament is either of length L^* and clamped at one end, normal to the flow and physical boundaries; or of length $2L^*$, tethered at its center, and assumed to deform symmetrically about the x^* axis. While our treatment will be for a general flow profile, we shall focus our results on the particular uniform, shear, and parabolic flow profiles depicted in Fig. 1 and defined in Table I; the first and third profiles correspond to the symmetric-deformation scenario, while the second profile corresponds to the clamped-end scenario.

A key assumption underpinning our paper is that the filament is slender, such that the aspect ratio $\epsilon = a^*/L^* \ll 1$, in which a^* is the radius of the filament. We shall adopt the theoretical framework developed in that limit by Pozrikidis [44]. In particular, we shall neglect the inertia of the filament and the fluid and represent the filament by its centerline $\mathbf{x}^*(s^*)$, parameterized by the arc length s^* measured from the origin where the filament is tethered. The derivative

$$\frac{d\mathbf{x}^*}{ds^*} = \mathbf{t} \tag{2}$$

defines the tangent unit vector $\mathbf{t}(s^*)$. Its evolution along the centerline is determined by the curvature $\kappa^*(s^*)$, according to the Frenet-Serret relations,

$$\frac{d\mathbf{t}}{ds^*} = -\kappa^* \mathbf{n}, \tag{3a}$$

$$\frac{d\mathbf{n}}{ds^*} = \kappa^* \mathbf{t}, \tag{3b}$$

TABLE I. The flows $\mathbf{u}_\infty^* = u^*(y^*)\hat{\mathbf{e}}_y$ depicted in Fig. 1: Dimensional flow profile $u^*(y^*)$, characteristic speed U^* corresponding to the maximal flow speed over the nominal configuration of the filament, and dimensionless flow profile $u(y)$.

	Uniform flow	Shear flow	Parabolic flow
$u^*(y^*)$	U^*	$\dot{\gamma}^* y^*$	$-\left(\frac{dp}{dx}\right)^* \frac{H^{*2}}{8\mu^*}\left(1 - \frac{4y^{*2}}{H^{*2}}\right)$
U^*	U^*	$\dot{\gamma}^* L^*$	$-\left(\frac{dp}{dx}\right)^* \frac{H^{*2}}{8\mu^*}$
$u(y)$	1	y	$1 - \frac{4y^2}{H^2}$

where choosing the normal unit vector $\mathbf{n}(s^*)$ as $\mathbf{n} = \hat{\mathbf{e}}_z \times \mathbf{t}$ determines the sign of $\kappa^*(s^*)$ and makes (3b) redundant. Furthermore, introducing the angle $\vartheta(s^*)$ between $\mathbf{t}(s^*)$ and $\hat{\mathbf{e}}_x$ reduces (3) to

$$\frac{d\vartheta}{ds^*} = -\kappa^*. \tag{4}$$

Since the inertia of the filament is neglected, the elastic and hydrodynamic forces acting on an infinitesimal section of the filament must balance. Denoting the cross-sectionally averaged internal force by $\mathbf{F}^*(s^*)$ and the hydrodynamic force per-unit length by $\mathbf{f}^*(s^*)$, we accordingly have that

$$\frac{d\mathbf{F}^*}{ds^*} + \mathbf{f}^* = \mathbf{0}. \tag{5}$$

In the slender-body limit, and for Stokes flow, $\mathbf{f}^*(s^*)$ can be approximated as

$$\mathbf{f}^* = \mathbf{R}^* \cdot \mathbf{u}_\infty^*, \tag{6}$$

in which

$$\mathbf{R}^* = \frac{4\pi\mu^*}{\ln 1/\epsilon}\left(\mathbf{I} - \frac{1}{2}\mathbf{t}\mathbf{t}\right) \tag{7}$$

is a resistance tensor, $\mathbf{I}$ being the identity tensor, and $\mathbf{u}_\infty^*$ is provided by (1) evaluated at $y^* = \hat{\mathbf{e}}_y \cdot \mathbf{x}^*(s^*)$. We note that (6) corresponds to a local slender-body approximation that neglects the disturbance to the fluid flow owing to the presence of the filament as well as physical boundaries (whose contributions are of order $O(1/\ln^2 \epsilon^{-1})$ [18].

It is convenient to decompose the internal force into tangential and normal components, denoted by T^* and N^*, respectively, so that

$$\mathbf{F}^* = T^*\mathbf{t} + N^*\mathbf{n}. \tag{8}$$

The force balance can then be rewritten using the Frenet-Serret relations (3) as

$$\left(\frac{dN^*}{ds^*} - \kappa^* T^*\right)\mathbf{n} + \left(\frac{dT^*}{ds^*} + N^*\kappa^*\right)\mathbf{t} + \mathbf{f}^* = \mathbf{0}. \tag{9}$$

In addition to the force balance, we require the differential torque balance,

$$\frac{dM^*}{ds^*} - N^* = 0, \tag{10}$$

where M^* is the internal bending moment in the filament. It can be expressed in terms of the curvature κ^* as $M^* = E^*I^*\kappa^*$, wherein E^* is the elastic modulus and I^* is the second areal moment of inertia, such that (10) gives

$$\frac{d\kappa^*}{ds^*} = \frac{N^*}{E^*I^*}. \tag{11}$$

From symmetry considerations, we can treat the clamped-end and symmetric-deformation scenarios simultaneously by prescribing clamped-end conditions at the tether point and considering positive s^*. Thus, the formulation is closed by prescribing the clamped-end boundary conditions

$$\mathbf{x}^*(0) = \mathbf{0}, \tag{12a}$$

$$\vartheta(0) = \pi/2, \tag{12b}$$

and the free-end boundary conditions:

$$T^*(L^*) = 0, \tag{13a}$$

$$N^*(L^*) = 0, \tag{13b}$$

$$\kappa^*(L^*) = 0. \tag{13c}$$

B. Dimensionless formulation

It will be convenient to normalize lengths by L^*, velocities by U^*, defined as the maximal speed over the nominal configuration of the filament (Table I), forces by $4\pi \mu^* L^* U^* / \ln \epsilon^{-1}$ and moments by the latter times L^*. Dimensionless quantities will be denoted similarly to before, with the asterisk omitted. With a slight abuse of notation, we decompose the centerline position as $\mathbf{x}(s) = x(s)\hat{\mathbf{e}}_x + y(s)\hat{\mathbf{e}}_y$. The problem formulation above can then be seen to reduce to the set of ordinary differential equations,

$$\frac{dT}{ds} + \kappa N = -\frac{u(y)}{2}\cos\vartheta, \tag{14a}$$

$$\frac{dN}{ds} - \kappa T = u(y)\sin\vartheta, \tag{14b}$$

$$\frac{d\kappa}{ds} = \eta N, \tag{14c}$$

$$\frac{d\vartheta}{ds} = -\kappa, \tag{14d}$$

$$\frac{dx}{ds} = \cos\vartheta, \tag{14e}$$

$$\frac{dy}{ds} = \sin\vartheta, \tag{14f}$$

which are supplemented by the clamped-end boundary conditions,

$$x(0) = 0, \tag{15a}$$

$$y(0) = 0, \tag{15b}$$

$$\vartheta(0) = \pi/2, \tag{15c}$$

and the free-end boundary conditions:

$$T(1) = 0, \tag{16a}$$

$$N(1) = 0, \tag{16b}$$

$$\kappa(1) = 0. \tag{16c}$$

The above dimensionless formulation involves a compliance parameter,

$$\eta = \frac{4\pi \mu^* L^{*3} U^*}{E^* I^* \ln 1/\epsilon}, \tag{17}$$

which characterizes the relative strength of viscous forces to elastic (bending) forces. The latter quantity is sometimes referred to as the Sperm number [45]. It is the only dimensionless parameter in the problem, besides any parameters involved in prescribing the flow profile $u(y)$. The dimensionless flow profiles corresponding to the uniform, shear, and parabolic flows are provided in Table I. As a consequence of the x independence of the flow profile, the above problem can be separated into two subsequent steps. First, the differential equations (14a)–(14d) and (14f) can be integrated in conjunction with the boundary conditions (15b), (15c), and (16) to obtain $y(s)$, $\vartheta(s)$, $T(s)$, $N(s)$, and $\kappa(s)$. Having obtained $\vartheta(s)$, the differential equation (14e) can then be integrated, in conjunction with the initial condition (15a), to find $x(s)$.

Numerically, we have implemented an iterative shooting method in Python, which incorporates continuation to access a wide range of η values. Analytically, we shall derive in Secs. III and IV closed-form approximations in the limits $\eta \ll 1$ and $\eta \to \infty$, respectively. In Sec. V, we shall apply our asymptotic predictions for a general flow profile $u(y)$ to the uniform, shear, and parabolic flows, and find good agreement with numerical results. We give concluding remarks in Sec. VI.

III. SMALL COMPLIANCES

For $\eta \ll 1$, we expect small deformations of the filament from its nominal shape: $x(s) = 0$, $y(s) = s$, $\kappa(s) = 0$, and $\vartheta(s) = \pi/2$. For any smooth flow profile $u(y)$, the governing equations suggest regular perturbation expansions in powers of η of the form

$$x(s; \eta) = \eta X_1(s) + \eta^3 X_3(s) + \cdots, \tag{18a}$$

$$y(s; \eta) = s + \eta^2 Y_2(s) + \cdots, \tag{18b}$$

$$T(s; \eta) = \eta T_1(s) + \eta^3 T_3(s) + \cdots, \tag{18c}$$

$$N(s; \eta) = N_0(s) + \eta^2 N_2(s) + \cdots, \tag{18d}$$

$$\kappa(s; \eta) = \eta \kappa_1(s) + \eta^3 \kappa_3(s) + \cdots, \tag{18e}$$

$$\vartheta(s; \eta) = \frac{\pi}{2} + \eta \vartheta_1(s) + \eta^3 \vartheta_3(s) + \cdots, \tag{18f}$$

with the flow profile possessing the corresponding expansion:

$$u(y(s; \eta)) = u(s) + \eta^2 \left. \frac{du}{dy} \right|_{y=s} Y_2(s) + \cdots. \tag{19}$$

We observe that $x(s; \eta)$, $T(s; \eta)$, and $\kappa(s; \eta)$ are odd functions in η, while $y(s; \eta)$ and $N(s; \eta)$ are even functions in η. Substituting the perturbation expansions into the set of differential equations (14), and boundary conditions (15) and (16), yields a sequence of closed problems that, at least in principle, could be solved iteratively.

Terms up to order η can be obtained by sequentially solving the three first-order equations

$$\frac{dN_0}{ds} = u(s), \quad N_0(1) = 0; \tag{20a}$$

$$\frac{d\kappa_1}{ds} = N_0, \quad \kappa_1(1) = 0; \tag{20b}$$

$$\frac{d\vartheta_1}{ds} = -\kappa_1, \quad \vartheta_1(0) = 0; \tag{20c}$$

after which both of the following first-order equations can be solved:

$$\frac{dT_1}{ds} + \kappa_1 N_0 = \frac{1}{2} u(s) \vartheta_1, \quad T_1(1) = 0; \tag{21a}$$

$$\frac{dX_1}{ds} = -\vartheta_1, \quad X_1(0) = 0. \tag{21b}$$

Terms up to η^3 can be obtained similarly by sequentially solving the set of equations

$$\frac{dY_2}{ds} = -\frac{\vartheta_1^2}{2}, \quad Y_2(0) = 0; \tag{22a}$$

$$\frac{dN_2}{ds} - \kappa_1 T_1 = u'(s) Y_2 - u(s) \frac{\vartheta_1^2}{2}, \quad N_2(1) = 0; \tag{22b}$$

$$\frac{d\kappa_3}{ds} = N_2, \quad \kappa_3(1) = 0; \tag{22c}$$

$$\frac{d\vartheta_3}{ds} = -\kappa_3, \quad \vartheta_3(0) = 0; \tag{22d}$$

after which both of the following equations can be solved:

$$\frac{dT_3}{ds} + \kappa_3 N_0 + \kappa_1 N_2 = \frac{1}{2}\left[u(s)\left(\vartheta_3 - \frac{\vartheta_1^3}{6}\right) + u'(s)Y_2\vartheta_1\right], \quad T_3(1) = 0; \tag{23a}$$

$$\frac{dX_3}{ds} = -\left(\vartheta_3 - \frac{\vartheta_1^3}{6}\right), \quad X_3(0) = 0. \tag{23b}$$

We have solved (20)–(23), using MATHEMATICA [46], for the uniform, shear and parabolic flow profiles. Explicit solutions up to order η are provided in Appendix A; expressions for the order η^2 and η^3 fields are omitted, owing to their length, however they will be included in the results of Sec. V.

IV. LARGE COMPLIANCES

A. Scalings and form of outer approximation

For $\eta \gg 1$, we expect that the filament strongly bends toward the direction of the flow, such that $y \ll 1$ all along the filament. Accordingly, only the small-y behavior of the prescribed flow profile $u(y)$ should be important; to leading order, we assume that this behavior possesses the power-law form

$$u(y) \sim u_\alpha y^\alpha \quad \text{as} \quad y \searrow 0, \tag{24}$$

where $\alpha \geqslant 0$ is an arbitrary exponent and, without loss of generality (as the direction of the x axis can be flipped), we shall assume that $u_\alpha > 0$. Note that $\alpha = 0$ for the uniform and parabolic profiles and $\alpha = 1$ for the shear profile, with $u_\alpha = 1$ for all three profiles (Table II). Thus, the leading-order behavior (24) is identical for the uniform and parabolic flow and, as a consequence, so will our predictions be for the leading-order filament shape as $\eta \to \infty$.

Asymptotically, we find that there are two regions: a filament-scale outer region, corresponding to holding $s \in (0, 1]$ fixed as $\eta \to \infty$, and an inner region near the clamped point, corresponding to the asymptotic region $s = O(\delta(\eta))$, wherein $\delta(\eta) \ll 1$ is a scaling to be determined.

Consider first the outer region, where the smallness of y suggests $\vartheta, \kappa \ll 1$. By inspecting the form of the governing equations (14), considered together with the free-end boundary conditions (16), we conclude that ϑ, κ, and N must, in fact, be *exponentially small* in the outer limit. Given the asymptotic smallness of ϑ, it follows from (14f) that y is constant to exponential order, viz.,

$$y(s; \eta) \approx \bar{y}(\eta), \tag{25}$$

where $\bar{y}(\eta) \ll 1$ is constant in s and we will use $\approx$ to indicate an exponentially small absolute error as $\eta \to \infty$. We also define the leading-order approximation of $\bar{y}(\eta)$ as

$$\bar{y}(\eta) \sim \lambda(\eta)\psi, \tag{26}$$

in which ψ is a constant and $\lambda(\eta) \ll 1$ a scaling. Similarly, from (14e) we find

$$x(s; \eta) \approx s + \bar{x}(\eta), \tag{27}$$

where $\bar{x}(\eta) \ll 1$ is constant in s.

Using the exponential smallness of ϑ and κN, as well as (25), we can exponentially approximate (14a) as

$$\frac{dT}{ds} \approx -\frac{\bar{u}(\eta)}{2}, \tag{28}$$

where we define

$$\bar{u}(\eta) = u(\bar{y}(\eta)), \tag{29}$$

for which a leading-order approximation is $u_\alpha \lambda^\alpha(\eta) \psi^\alpha$. Using the free-end boundary condition (16a), we can integrate (28) to find

$$T(s; \eta) \approx \frac{\bar{u}(\eta)}{2}(1 - s). \tag{30}$$

In particular, to leading order we write

$$T(s; \eta) \sim \lambda^\alpha(\eta)(1 - s)\omega, \tag{31}$$

where we define the constant

$$\omega = \frac{u_\alpha \psi^\alpha}{2}. \tag{32}$$

Turning to the inner region, the boundary condition (15c) suggests that ϑ is order unity there, while the outer approximation (26), which is constant in s, suggests that y is order $\lambda(\eta)$ also in the inner region; (14f) therefore implies that the scalings $\delta(\eta)$ and $\lambda(\eta)$ are comparable. Furthermore, the outer approximation (31), which is regular at $s = 0$, suggests that T is also order λ^α in the inner region; (14d) suggests that κ is order $1/\delta$ and (14c) suggests that N is order $\eta^{-1}\delta^{-2}$. In (14a) and (14b), the hydrodynamic right-hand sides are order λ^α, negligible relative to dT/ds, and $-\kappa T$, respectively, which are order $\lambda^{\alpha-1}$. The balance of elastic terms in those equations thus yields the scaling result:

$$\delta(\eta), \lambda(\eta) = \eta^{-1/(\alpha+2)}. \tag{33}$$

We note that the choice of a unity prefactor on the right-hand side of (33) fixes the definition of ψ (and ω).

B. Inner approximation

To study the inner region, we define the strained arc length

$$S = \eta^{1/(\alpha+2)}s, \tag{34}$$

and corresponding fields

$$x(s; \eta) = \eta^{-1/(\alpha+2)}X(S; \eta), \tag{35a}$$

$$y(s; \eta) = \eta^{-1/(\alpha+2)}Y(S; \eta) \tag{35b}$$

$$T(s; \eta) = \eta^{-\alpha/(\alpha+2)}\mathcal{T}(S; \eta), \tag{35c}$$

$$N(s; \eta) = \eta^{-\alpha/(\alpha+2)}\mathcal{N}(S; \eta) \tag{35d}$$

$$\kappa(s; \eta) = \eta^{1/(\alpha+2)}\mathcal{K}(S; \eta), \tag{35e}$$

$$\vartheta(s; \eta) = \Theta(S; \eta), \tag{35f}$$

where we have rescaled according to (33) and the discussion preceding that equation. The rescaled inner fields are expected to possess η-independent leading-order approximations, i.e.,

$$\mathcal{F}(S; \eta) = \mathcal{F}_0(\eta) + \cdots, \tag{36}$$

in the inner limit $\eta \to \infty$ with $S > 0$ fixed.

From (14), the leading-order inner fields defined by (35) satisfy the differential equations

$$\frac{d\mathcal{T}_0}{dS} + \mathcal{K}_0\mathcal{N}_0 = 0, \tag{37a}$$

$$\frac{d\mathcal{N}_0}{dS} - \mathcal{K}_0\mathcal{T}_0 = 0, \tag{37b}$$

$$\frac{d\mathcal{K}_0}{dS} = \mathcal{N}_0, \tag{37c}$$

$$\frac{d\Theta_0}{dS} = -\mathcal{K}_0, \tag{37d}$$

$$\frac{dX_0}{dS} = \cos\Theta_0, \tag{37e}$$

$$\frac{dY_0}{dS} = \sin\Theta_0, \tag{37f}$$

which describe bending of the filament in the absence of external forces. These differential equations are to be solved in conjunction with the clamped-end boundary conditions

$$X_0(0) = 0, \tag{38a}$$

$$Y_0(0) = 0, \tag{38b}$$

$$\Theta_0(0) = \pi/2, \tag{38c}$$

which follow from (15), and the matching conditions

$$Y_0(S) \to \psi, \tag{39a}$$

$$\mathcal{T}_0(S) \to \omega, \tag{39b}$$

$$\mathcal{K}_0(S) \to 0, \tag{39c}$$

$$\Theta_0(S) \to 0 \quad \text{as} \quad S \to \infty. \tag{39d}$$

The first two conditions are implied by the leading-order outer approximations (26) and (31), while the latter two follow from the smallness of κ and ϑ in the outer region.

Substituting (37c) into (37a) and integrating using the matching conditions (39b) and (39c), we find

$$\mathcal{T}_0 + \tfrac{1}{2}\mathcal{K}_0^2 = \omega. \tag{40}$$

Next, we differentiate (37c) and substitute (37b) and (40) to find

$$\frac{d^2\mathcal{K}_0}{dS^2} = \mathcal{K}_0\left(\omega - \frac{1}{2}\mathcal{K}_0^2\right). \tag{41}$$

Integrating once gives

$$\left(\frac{d\mathcal{K}_0}{dS}\right)^2 = \mathcal{K}_0^2\left(\omega - \frac{1}{4}\mathcal{K}_0^2\right) + \text{const}, \tag{42}$$

where the integration constant must vanish given the matching condition (39c). We find the separable equation

$$\frac{d\mathcal{K}_0}{dS} = -\left(\omega - \frac{1}{4}\mathcal{K}_0^2\right)^{1/2}\mathcal{K}_0, \tag{43}$$

where the sign of the square root has been chosen such that $\mathcal{K}_0$ decays, rather than grows, monotonically. Integrating (43) yields the curvature profile

$$\mathcal{K}_0(S) = 2\omega^{1/2}\text{sech}(\omega^{1/2}S + \sigma), \tag{44}$$

where $\sigma > 0$ is an integration constant. Given (44), we find from (37c) and (40) that

$$\mathcal{N}_0(S) = -2\omega\,\text{sech}(\omega^{1/2}S + \sigma)\tanh(\omega^{1/2}S + \sigma), \tag{45a}$$

$$\mathcal{T}_0(S) = \omega(1 - 2\,\text{sech}^2(\omega^{1/2}S + \sigma)). \tag{45b}$$

TABLE II. Input parameters for the asymptotic expansions as $\eta \to \infty$, corresponding to the uniform, shear, and parabolic flow profiles. The exponent α and prefactor u_α describe the behavior of the flow profile near the tether point in accordance with the power law (24). The constant ψ corresponds to a leading-order approximation for the approximately uniform y value away from the clamped end [scaled by $\eta^{-1/(\alpha+2)}$]. The constant $\omega = 2/\psi^2$ is a matching parameter, which gives a leading-order approximation for the maximum tension force in the filament [scaled by $\eta^{-\alpha/(\alpha+2)}$].

	Uniform flow	Shear flow	Parabolic flow
α	0	1	0
u_α	1	1	1
ψ	2	$2^{2/3}$	2
ω	1/2	$2^{-1/3}$	1/2

The constant σ can be determined, along with an inner approximation for the geometry of the filament, by solving the problem governing $\Theta_0(S)$, which consists of the first-order differential equation (37d), the boundary condition (38c), and the matching condition (39d). We thereby find

$$\Theta_0(S) = 4\cot^{-1}\exp(\omega^{1/2}S + \sigma), \tag{46}$$

with

$$\sigma = \ln\cot\frac{\pi}{8} \doteq 0.8814\ldots. \tag{47}$$

With $\Theta_0(S)$ given by (46), the geometric profiles $X_0(S)$ and $Y_0(S)$ are found by integrating (37e) and (37f), employing the boundary conditions (38a) and (38b), as

$$X_0(S) = S + \sqrt{\frac{2}{\omega}}\{1 - 2^{1/2}\tanh(\omega^{1/2}S + \sigma)\}, \tag{48a}$$

$$Y_0(S) = \sqrt{\frac{2}{\omega}}\{1 - 2^{1/2}\text{sech}(\omega^{1/2}S + \sigma)\}. \tag{48b}$$

The constant ψ follows by applying the matching condition (39a) to the latter solution. This gives $\psi = \sqrt{2/\omega}$ or, more explicitly, using (32) for ω:

$$\psi = \left(\frac{4}{u_\alpha}\right)^{1/(2+\alpha)}. \tag{49}$$

The specific parameters (α, u_α, ψ, and ω) for the uniform, shear, and parabolic profiles are provided in Table II and can be substituted into the general solutions for the geometric features and forces acting on the filament. As anticipated, our leading-order large-η approximations are identical for the uniform and parabolic flow profiles. We also observe from (45b) that $\mathcal{T}_0(0) = 0$, since the constant σ, provided by (47), can also be expressed as arcsinh(1). This vanishing of the leading-order tension profile at the tether point is coincidental rather than corresponding to a boundary condition. We have no reason to expect higher-order terms in an expansion for the tension profile to also vanish at the tether point; indeed, the numerical results presented in Sec. V demonstrate that for large η the tension there is generally small, but does not vanish.

From this point, it is conceptually straightforward to extend the present large-η analysis to higher algebraic orders. Indeed, the forms of the outer approximations have been determined up to exponentially small errors. Thus, in the inner region we can solve, say numerically, a sequence of higher-order inner problems, which are linear and made determined, together with corresponding

terms in an expansion for $\bar{y}(\eta)$, via asymptotic matching with (26) and (28). We demonstrate this in Appendix B for the shear-flow profile, motivated by the fact that for that profile, but not for the uniform and parabolic profiles, the calculation of leading-order approximations for exponentially small quantities associated with the outer region demands knowledge of the first algebraic correction to $\bar{y}(\eta)$ (see Sec. IV E). Thus, we will need the result that, for the shear-flow profile,

$$\bar{y}(\eta) \sim \psi \eta^{-1/3} + \tilde{\psi} \eta^{-2/3}, \tag{50}$$

with $\tilde{\psi} \doteq 0.693\ldots$.

C. Longitudinal displacement

Consider the longitudinal displacement of the free end of the filament along the x axis, for which (27) gives the exponentially accurate, albeit uninformative, approximation:

$$x(1; \eta) \approx 1 + \bar{x}(\eta). \tag{51}$$

A leading approximation for $\bar{x}(\eta) \ll 1$ can be obtained via asymptotic matching between a two-term outer expansion and a leading-order inner expansion for x. Alternatively, matching can be avoided by considering the exact integral

$$x(1; \eta) = 1 - \int_0^1 (1 - \cos\vartheta)\, ds, \tag{52}$$

which follows from integration of (14e) using the boundary condition (15a). Since ϑ is exponentially small in the outer region, the integral is dominated by the inner region and is most easily evaluated to leading order using (37e) and the inner approximation (48a). Using either approach, we find

$$1 - x(1; \eta) \sim \eta^{-1/(\alpha+2)} \lim_{S \to \infty} \{S - X_0(S)\} = \eta^{-1/(\alpha+2)} \sqrt{\frac{2}{\omega}} (\sqrt{2} - 1). \tag{53}$$

D. Composite approximation for the tension

A leading-order composite approximation for the tension profile can be obtained by summing the outer approximation (31) and the inner approximation (45b), and subtracting their asymptotic overlap, namely, the limiting constant value of both approximations as either $s \searrow 0$ or $S \to +\infty$. This gives the composite approximation

$$T_{\text{comp}} = \eta^{-\alpha/(\alpha+2)} \omega \{1 - s - 2\,\text{sech}^2(\omega^{1/2} \eta^{1/(\alpha+2)} s + \sigma)\}, \tag{54}$$

which describes both the linear variation of the tension in the outer region, and its exponential behavior in the inner region. A leading-order composite approximation for the other fields is simply given by their respective leading-order inner approximations, as in the outer region all other fields are either exponentially small or, in the case of y, constant.

E. Exponential approximation for the filament slope at the free end

In the outer region, the filament is straight and aligned with the flow up to exponentially small orders. A leading-order approximation for the exponentially small deviations of the filament from a straight configuration can be determined with a Wentzel-Kramers-Brillouin (WKB) approach, despite these deviations being beyond all orders of the asymptotic expansions for the outer fields y and T, which we have actually only fully determined to leading order.

Starting from the differential equations (14b)–(14d), and using the exponential outer approximations (25) and (30), we find that, away from the tethered point, the angle ϑ satisfies the exponentially accurate differential equation

$$\frac{1}{\eta} \frac{d^3\vartheta}{ds^3} - \frac{\bar{u}(\eta)}{2}(1-s)\frac{d\vartheta}{ds} + \bar{u}(\eta)\vartheta \approx 0. \tag{55}$$

This equation is supplemented by the boundary conditions

$$\frac{d\vartheta}{ds} = 0, \tag{56a}$$

$$\frac{d^2\vartheta}{ds^2} = 0 \quad \text{at} \quad s = 1, \tag{56b}$$

which follow from the free-end conditions (16b) and (16c), as well as asymptotic matching with the inner region as $s \searrow 0$. An obvious quantity of interest is a leading-order approximation for ϑ at the free end $s = 1$.

The analysis is based on matching a WKB-type approximation for $0 < s < 1$ with the inner approximation as $s \searrow 0$, and with a free-end inner region near $s = 1$, which is necessary to satisfy the boundary conditions at the free end. The details of this calculation are relegated to Appendix C.

The uniform- and parabolic-flow cases, for which $\bar{u}(\eta) \equiv 1 + O(1/\eta)$, are again equivalent to leading order. We find

$$\vartheta(1; \eta) \sim \frac{\beta}{\eta^{1/12}} \exp\left(-\frac{\sqrt{2}}{3} \eta^{1/2}\right), \tag{57}$$

in which

$$\beta = \frac{2^{1/12} 8 \sqrt{\pi} \tan \frac{\pi}{8}}{3^{5/6} \Gamma(4/3)} \doteq 2.790 \ldots . \tag{58}$$

Consider now the shear-flow case, where $\bar{u}(\eta) = \bar{y}(\eta)$. The analysis of this case is slightly more involved, as the leading-order WKB approximation for $0 < s < 1$, and hence approximation for $\vartheta(1; \eta)$, turns out to depend on the first algebraic correction to $\bar{y}(\eta)$ [cf. (50)]. We find in Appendix C the result

$$\vartheta(1; \eta) \sim \frac{\beta_s}{\eta^{1/18}} \exp\left(-\frac{2^{5/6}}{3} \eta^{1/3}\right), \tag{59}$$

in which

$$\beta_s = \frac{\beta}{2^{1/18}} \exp\left(-\frac{\tilde{\psi}}{2^{5/6}3}\right) \doteq 2.358 \ldots . \tag{60}$$

V. DISCUSSION

We here discuss our predictions for the deformation of a slender filament in the uniform-, shear-, and parabolic-flow scenarios shown in Fig. 1. We start by studying the stationary geometric shape of the slender filament in each scenario, see Fig. 2. The flows induce a deformation of the tethered filament depending on the dimensionless compliance η [cf. (17)]. For numerically small η values, the filament remains almost perpendicular to the flow; the deformation is mostly appreciable near the free end of the filament. In this regime, our perturbation solutions for $\eta \ll 1$ agree well with our numerical solutions and describe the shape of the filament for all flows, even for $\eta \approx 1$. Furthermore, the filament shapes for the shear flow agree qualitatively with those presented in Ref. [44], where a nonlocal slender-body theory was employed that accounts for hydrodynamic interactions with the wall. For numerically large values of η, the filament is strongly bent at the tether point and aligns with the flow near the free end. In this regime, we find good agreement with the asymptotic approximations developed in the limit $\eta \to \infty$. In particular, the y coordinate of the free end scales as $\eta^{-1/2}$ for the uniform and parabolic flows [Figs. 2(a), 2(c), and 2(d)], and as $\eta^{-1/3}$ for the shear flow [Fig. 2(b)]. As these scalings become comparable to ϵ, slender-body theory fails owing to near-field interactions of the filament with itself (in the uniform- and parabolic-flow scenarios) or the wall (in the shear-flow scenario). This is not a stringent limitation, however, as even for, say,
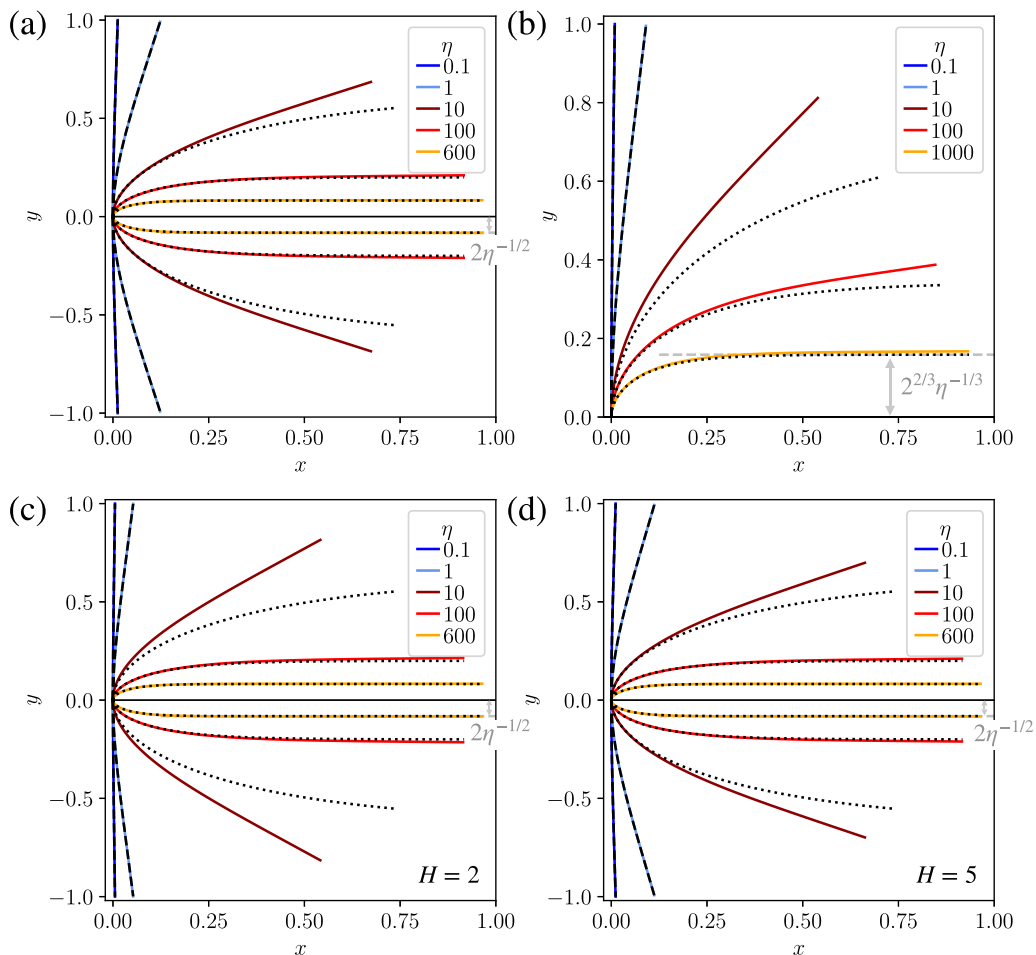
FIG. 2. Stationary filament shape (x, y) for (a) uniform flow, (b) shear flow, and (c), (d) parabolic flow, with $H = 2$ and $H = 5$, for the indicated values of η. Solid curves are numerical results. Dashed curves correspond to our regular-perturbation expansions for $\eta \ll 1$ (including terms up to order η^3). Dotted curves correspond to leading-order asymptotic approximations as $\eta \to \infty$; for the case of T the composite approximation (54) is shown. The gray dashed lines indicate the asymptotic values $\psi \eta^{-1/(\alpha+2)}$ for the uniform outer approximation for y.

$\eta = 600$, the dimensionless separation for the different flow scenarios is much larger than typical values of the aspect ratio, i.e., $y(1) \approx 0.1 \gg \epsilon \ (\approx 0.01)$.

To further address the dependence of the filament geometry on the compliance, we next discuss the variation with η of several key geometric quantities. Consider first the displacement $x(s = 1)$ of the free end of the filament along the flow; in Fig. 3(a) we plot numerical predictions for $1 - x(s = 1)$ as a function of η, alongside our asymptotic approximations for small and large η. We note that as $\eta \to \infty$ the data for the uniform and parabolic flows (with $H = 2$ or 5) collapse on a common asymptotic approximation, which scales as $\eta^{-1/2}$. The details of the flow profile become important at intermediate compliances $1 \lesssim \eta \lesssim 10$, where the extension for the uniform flow increases faster than for the parabolic flow. With increasing H and η, the parabolic-flow profile experienced by the filament becomes approximately uniform; in particular, we observe that the displacement for the parabolic flow with $H = 5$ is almost identical to that for the uniform flow for all η, while the
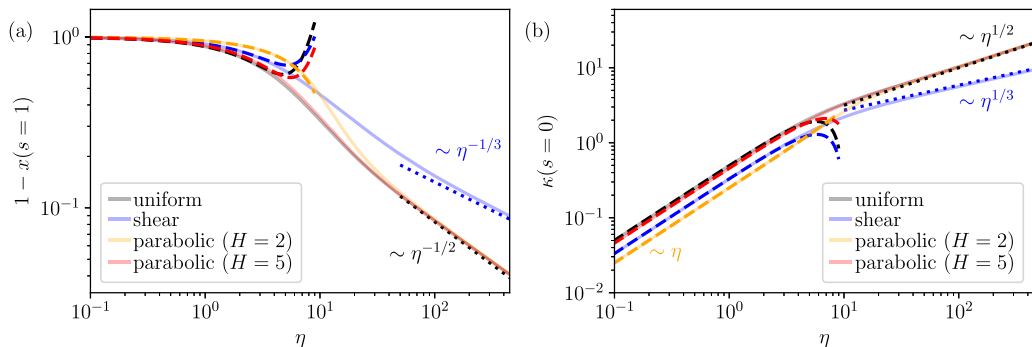
FIG. 3. Longitudinal extension (a) and curvature (b) at the tether point, as a function of η, for the indicated flow profiles. Solid curves are numerical results. Dashed curves correspond to our regular-perturbation expansions for $\eta \ll 1$ (including terms up to order η^3). Dotted curves correspond to leading-order asymptotic approximations as $\eta \to \infty$; note that the black dotted line corresponds to both the uniform and parabolic flow profiles, for which the leading-order large-η asymptotics are identical.

results for the parabolic flow with $H = 2$ collapse on those for the uniform flow only at large η. As predicted by the asymptotic theory, for the shear flow we find at large η the different scaling $\eta^{-1/3}$.

Another quantity for characterizing the shape of the filament is its curvature at the tether point; in Fig. 3(b), we plot numerical predictions for $\kappa(s = 0)$ as a function of η alongside our asymptotic approximations for small and large η. For $\eta \ll 1$, where the filament is barely bent, we find a linear increase of that curvature, irrespective of the flow profile, which is smallest for the parabolic flow with $H = 2$, followed by the shear flow, and largest for the uniform flow. For $\eta \gg 1$, the filament becomes more strongly bent near the tether point, which can be characterized by an increase in the curvature at the tether point. This curvature scales as $\eta^{1/2}$ for the uniform and parabolic flows and $\eta^{1/3}$ for the shear flow.

In Figs. 5(a) (i)–5(c)(i), we plot numerical and asymptotic predictions for the filament curvature as a function of arc length s. This demonstrates that the curvature decreases monotonically along the filament, from its value at the tether point, discussed above, to zero at the free end. For $\eta \gg 1$,
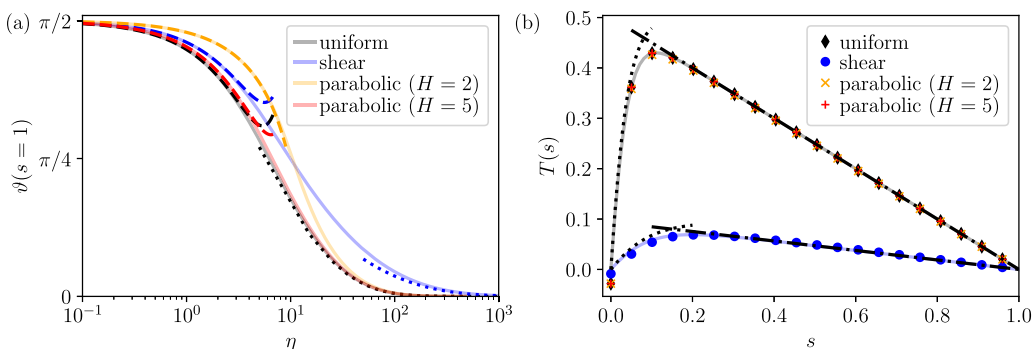

FIG. 4. (a) Angle ϑ at the free end $s = 1$, for the indicated flow profiles. Solid curves are numerical results. Dashed curves depict our regular-perturbation expansions for $\eta \ll 1$ (including terms up to order η^3). Dotted curves depict our leading-order exponential approximations as $\eta \to \infty$, which are identical for the uniform and parabolic flows. (b) Tangential-force profile $T(s)$ for $\eta = 50$, for uniform, shear and parabolic flows as indicated. Asymptotic predictions as $\eta \to \infty$: dashed curve is the leading-order 'outer' approximation, dotted curve is the leading-order 'inner' approximation, and solid curve is the leading-order 'composite' approximation. The leading-order asymptotic predictions are identical for uniform and parabolic flows. Symbols represent numerical results.
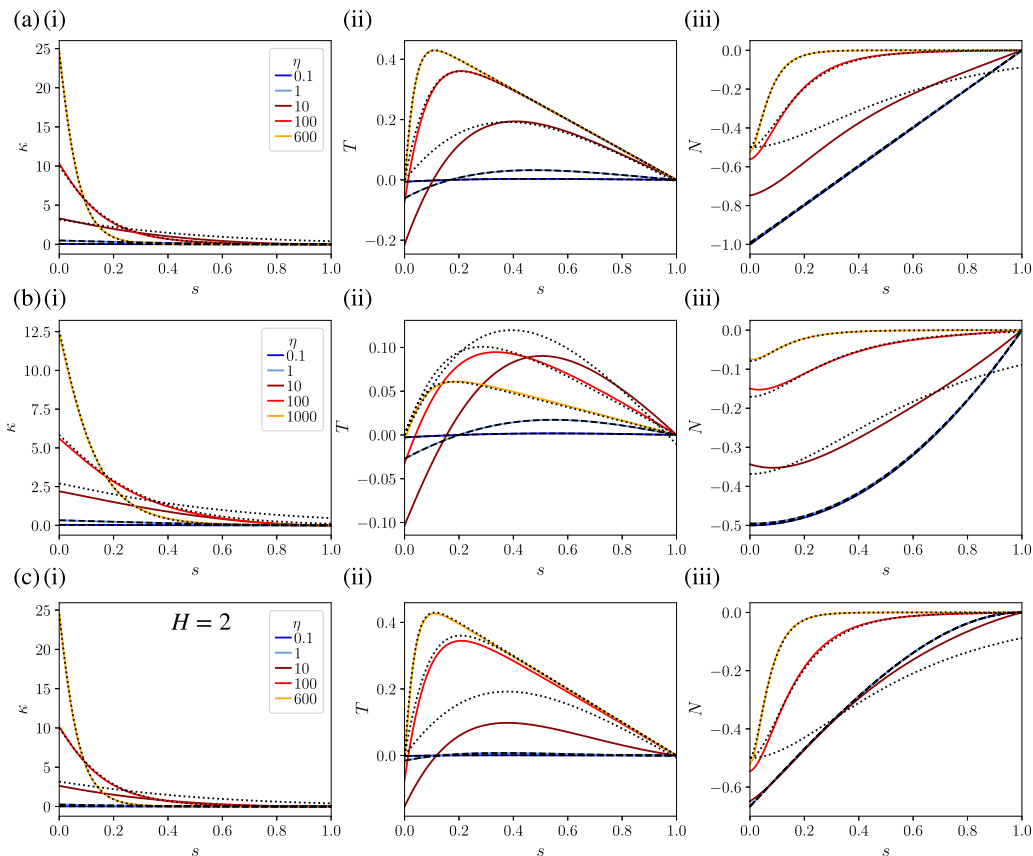
FIG. 5. Curvature $\kappa(s)$, tangential-force $T(s)$ and normal-force $N(s)$ profiles for (a) uniform flow; (b) shear flow; and (c) parabolic flow, with $H = 2$. Plotted as a function of the arc length s for the indicated values of η. Dashed curves correspond to our regular-perturbation expansions for $\eta \ll 1$ (including terms up to order η^3). Dotted curves correspond to leading-order asymptotic approximations as $\eta \to \infty$. For the case of T the composite approximation (54) is shown.

our asymptotic theory predicts that away from the tether point the curvature is exponentially small, and describes the nearly straight filament geometry in that region in terms of the exponentially small angle profile $\vartheta(s)$. In Fig. 4(a), we show the filament angle at the free end, $\vartheta(s = 1)$, as a function of η and for the various flow profiles. The good agreement at large η between our numerical data and the exponential asymptotic approximation serves to corroborate both the numerical method and the asymptotic theory.

Finally, our solutions provide access to the internal forces, T and N, acting, respectively, tangentially and normally to the filament backbone; numerical and asymptotic predictions are plotted in Figs. 5(a)(ii)–5(c)(iii). Irrespective of η, the tangential force is compressive near the tether point ($s = 0$) and extensional at intermediate s. The numerical data for the tension force agrees well with our asymptotic predictions for small and large η. In the latter limit, the comparison is made with the composite approximation (54), which is accurate all along the filament. As demonstrated in Fig. 4(b), this composite approximation combines an inner approximation near the tether point and a linear-in-s outer approximation valid away from the tether point. We note that the maximum of the tension represents roughly the edge between the inner and outer regions; this maximum tension is order unity for the uniform and parabolic flows, and small like $\eta^{-1/3}$ for the shear flow. The normal force, N, is directed toward the wall/plane of symmetry for all η, see Figs. 5(a)(iii)–5(c)(iii). Its
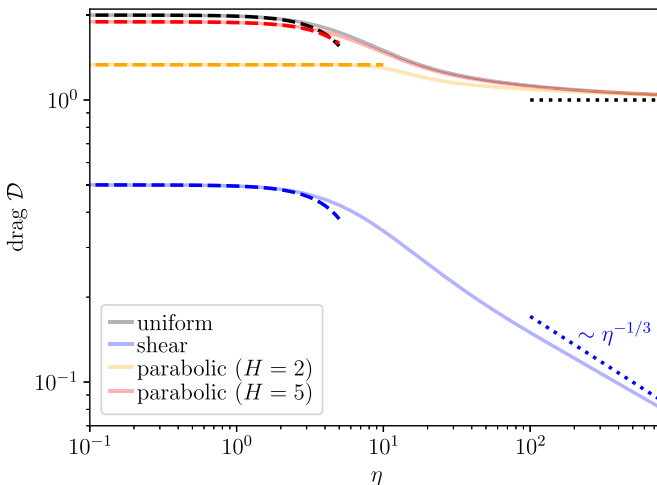
FIG. 6. Total drag $\mathcal{D}$ on the filament as a function of η for the indicated flow profiles. Solid curves are numerical results. Dashed curves correspond to our regular-perturbation expansions for $\eta \ll 1$ (including terms up to order η^3). Dotted curves correspond to leading-order asymptotic approximations as $\eta \to \infty$.

magnitude is seen to attenuate with η, for all s. This attenuation, however, is nonuniform in s for large η. As described by our asymptotic theory in that limit, the normal force becomes localized to the tether point, where it scales like the tension force; it is exponentially small away from the tether point where the filament is aligned with the direction of the flow. Incidentally, the total drag on the filament,

$$\mathcal{D} = \hat{\mathbf{e}}_x \cdot \int \mathbf{f} ds, \tag{61}$$

where the integral is over the length of the filament, can be related to the normal force component at the tether point. Substituting the force balance (5) into the above integral and using (8) together with the boundary conditions (12) and (13), we find $\mathcal{D} = -N(0)$ for shear flow and $\mathcal{D} = -2N(0)$ for the uniform and parabolic flow scenarios. The drag as a function of η is shown in Fig. 6. At large η, it approaches a constant for the uniform and parabolic flows, while for shear flow it decays as $\eta^{-1/3}$. We note that the total drag reduces only by a factor of $\sim 2 - 6$ as we vary η by roughly four orders in magnitude. In this context, we refer the reader to Ref. [47] for an analogous large-Reynolds-number analytical study of reduced drag on a filament deforming in uniform flow.

VI. CONCLUSIONS

We have presented the stationary geometrical properties and forces acting on a slender filament in different unidirectional flows. In our analysis, the filament is either clamped at one end perpendicularly to the background flow or tethered at its center and deforms symmetrically around the plane parallel to the flow. Besides the details of the background flow, the deformation of the filament only depends on the nondimensional compliance η, which measures the relative importance of viscous forces with respect to elastic forces. Using numerical solutions and asymptotic expansions for $\eta \ll 1$ and $\eta \to \infty$, we have rationalized scaling behaviors for the extension of the filament and the filament curvature with particular focus on uniform, shear, and parabolic background flows.

Our theoretical predictions cover the entire regime from small to large compliances. In particular, our analytical asymptotic approximations can be compared directly to experiments for slender bodies and allow measuring their elastic properties by, for example, comparing the filament extension

under flow. Furthermore, they represent the base case for studying Brownian effects present in small-scale systems, such as DNA [43] or cellular appendages [17].

The model adapted from Ref. [44] and our analytical framework is expected to serve as a reference system for studying numerous other scenarios involving slender filaments in flow. For example, it could be extended to account for the twisted structure of slender filaments and their stationary configuration in the presence of flows or internal driving [1,11]. The techniques established for deriving asymptotic expansions as $\eta \to \infty$ could be applied to investigate the shape of free filaments in background flows, the deformation of filament beds, or scenarios with multiple solutions and instabilities, such as the behavior of a clamped filament in a stagnation flow [38].

Finally, our theory is based on a leading-order slender-body approximation and thereby ignores nonlocal hydrodynamic interactions of the filament with itself and nearby boundaries. While such an approximation is asymptotically valid in the limit where the filament becomes increasingly slender, it involves a logarithmic asymptotic error that can be significant in relevant experimental systems [15,43]. Furthermore, the local approximation can formally break down at extremely large compliances for which distances between different segments of the filament or between segments of the filament and a boundary become comparable to the filament diameter. Future work should address these deficiencies by revisiting this analytical and numerical study with nonlocal effects included.

APPENDIX A: SMALL-η PERTURBATION EXPANSIONS FOR DIFFERENT FLOW FIELDS

1. Uniform flow

For $u(y) = 1$,

$$N_0 = s - 1, \tag{A1a}$$

$$\kappa_1 = \tfrac{1}{2}(s^2 - 2s + 1), \tag{A1b}$$

$$\vartheta_1 = \tfrac{1}{6}(-s^3 + 3s^2 - 3s), \tag{A1c}$$

$$T_1 = \tfrac{1}{48}(-7s^4 + 28s^3 - 42s^2 + 24s - 3), \tag{A1d}$$

$$X_1 = \tfrac{1}{24}(s^4 - 4s^3 + 6s^2). \tag{A1e}$$

2. Shear flow

For $u(y) = y$,

$$N_0 = \tfrac{1}{2}(s^2 - 1), \tag{A2a}$$

$$\kappa_1 = \tfrac{1}{6}(2 - 3s + s^3), \tag{A2b}$$

$$\vartheta_1 = \tfrac{1}{24}s(-8 + 6s - s^3), \tag{A2c}$$

$$T_1 = \tfrac{1}{288}(-8 + 48s - 36s^2 - 32s^3 + 33s^4 - 5s^6), \tag{A2d}$$

$$X_1 = \tfrac{1}{120}(20s^2 - 10s^3 + s^5), \tag{A2e}$$

3. Parabolic flow

For $u(y) = 1 - 4y^2/H^2$,

$$N_0 = -\frac{4(s^3 - 1)}{3H^2} + s - 1, \tag{A3a}$$

$$\kappa_1 = -\frac{(s-1)^2(-3H^2 + 2s(s+2) + 6)}{6H^2}, \tag{A3b}$$

$$\vartheta_1 = \frac{s}{30}\left(\frac{2(s^4 - 10s + 15)}{H^2} - 5((s-3)s + 3)\right), \tag{A3c}$$

$$\begin{aligned}
T_1 = \frac{1}{720H^4}(&-15H^4(s-1)(7s((s-3)s+3)-3) \\
&+4H^2(s-1)(s(s(s(s(41s-55)+20)-120)+255) \\
&-45) - 4(s(13s^7 - 128s^4 + 150s^3 + 160s - 240) + 45)),
\end{aligned} \tag{A3d}$$

$$X_1 = \frac{1}{360}s^2\left(-\frac{4(s^4 - 20s + 45)}{H^2} + 15(s-4)s + 90\right). \tag{A3e}$$

APPENDIX B: FIRST ALGEBRAIC CORRECTION AS $\eta \to \infty$ (SHEAR FLOW)

Consider the shear-flow profile, where $u(y) = y$ and so $\bar{u}(\eta) = \bar{y}(\eta)$. It is readily seen from (14) that the hydrodynamic force results in a perturbation of relative order $\eta^{-1/3}$. Accordingly, we extend the generic inner expansion (36) as

$$\mathcal{F}(S; \eta) = \mathcal{F}_0(S; \eta) + \eta^{-1/3}\mathcal{F}_1(S; \eta) + \cdots, \tag{B1}$$

and the expansion (26) for $\bar{y}(\eta)$ as

$$\bar{y}(\eta) = \eta^{-1/3}\psi + \eta^{-2/3}\tilde{\psi} + \cdots. \tag{B2}$$

From (14), the first-correction fields satisfy the differential equations

$$\frac{d\mathcal{T}_1}{dS} + \mathcal{K}_0\mathcal{N}_1 + \mathcal{K}_1\mathcal{N}_0 = -\frac{1}{2}Y_0\cos\Theta_0, \tag{B3a}$$

$$\frac{d\mathcal{N}_1}{dS} - \mathcal{K}_0\mathcal{T}_1 - \mathcal{K}_1\mathcal{T}_0 = Y_0\sin\Theta_0, \tag{B3b}$$

$$\frac{d\mathcal{K}_1}{dS} = \mathcal{N}_1, \tag{B3c}$$

$$\frac{d\Theta_1}{dS} = -\mathcal{K}_1, \tag{B3d}$$

$$\frac{dX_1}{dS} = -\Theta_1\sin\Theta_0, \tag{B3e}$$

$$\frac{dY_1}{dS} = \Theta_1\cos\Theta_0. \tag{B3f}$$

These differential equations are to be solved in conjunction with the boundary conditions

$$X_1(0) = 0, \tag{B4a}$$

$$Y_1(0) = 0, \tag{B4b}$$

$$\Theta_1(0) = 0, \tag{B4c}$$

which follow from (15), and the matching conditions

$$Y_1(S) \to \tilde{\psi}, \tag{B5a}$$

$$\mathcal{T}_1(S) + \frac{\psi}{2}S \to \frac{\tilde{\psi}}{2}, \tag{B5b}$$

$$\mathcal{K}_1(S) \to 0, \tag{B5c}$$

$$\Theta_1(S) \to 0 \quad \text{as} \quad S \to \infty. \tag{B5d}$$

The first two conditions are implied by the outer approximations (25) and (30), with (B2), while the latter two follow from the exponential smallness of κ and ϑ in the outer region.

The above linear problem determines the order $\eta^{-2/3}$ inner fields, together with the constant $\tilde{\psi}$. By solving this problem numerically, we find the result $\tilde{\psi} \doteq 0.693$ also stated in the main text.

APPENDIX C: ANALYSIS OF EXPONENTIALLY SMALL FILAMENT ANGLE AS $\eta \to \infty$

1. Uniform and parabolic flows

For both the uniform and parabolic flows, we have

$$\bar{u}(\eta) = 1 + O(\eta^{-1}) \quad \text{as} \quad \eta \to \infty, \tag{C1}$$

so the exponentially accurate differential equations (55) can be written as

$$\frac{1}{\eta}\frac{d^3\vartheta}{ds^3} - \frac{1}{2}[1 + O(\eta^{-1})](1 - s)\frac{d\vartheta}{ds} + [1 + O(\eta^{-1})]\vartheta \approx 0. \tag{C2}$$

A dominant-balance analysis of (C2) suggests an inner region of thickness order $1/\eta^{1/3}$ near the free end $s = 1$ [unrelated to the inner region near the tether point, wherein (55) does not hold]. To consider this free-end inner region, we define the strained arc length

$$\rho = \eta^{1/3}(1 - s), \tag{C3}$$

and expand

$$\vartheta(s; \rho) = \Phi(\rho; \eta) + \cdots, \tag{C4}$$

holding $\rho > 0$ fixed. From (C2), Φ satisfies the differential equation

$$\frac{d^3\Phi}{d\rho^3} - \frac{\rho}{2}\frac{d\Phi}{d\rho} - \Phi = 0, \tag{C5}$$

while (56) give the free-end boundary conditions

$$\frac{d\Phi}{d\rho} = 0, \tag{C6a}$$

$$\frac{d^2\Phi}{d\rho^2} = 0 \quad \text{at} \quad \rho = 0. \tag{C6b}$$

The solution to (C5) and (C6) is

$$\Phi(\rho; \eta) = \xi(\eta)\rho I_{-2/3}\left(\frac{\sqrt{2}}{3}\rho^{3/2}\right), \tag{C7}$$

where $I_{-2/3}$ is the modified Bessel function of the first kind, of order $-2/3$, and $\xi(\eta)$ is a prefactor to be determined along with its scaling with η, which we expect to be exponentially small. We shall

later need the behaviors [48]

$$I_{-2/3}(x) \sim \frac{1}{(2\pi x)^{1/2}} e^x \quad \text{as} \quad x \to +\infty, \tag{C8a}$$

$$I_{-2/3}(x) \sim \frac{2^{2/3}}{\Gamma(\frac{1}{3})x^{2/3}} \quad \text{as} \quad x \to 0. \tag{C8b}$$

To connect the inner region near $s = 0$ with the free-end inner region near $s = 1$, we use a WKB approach to approximate the solution to (C2) for $0 < s < 1$. Substituting the ansatz

$$\vartheta(s; \eta) \propto A(s; \eta) \exp[\eta^{1/2}\Psi(s)] \tag{C9}$$

into (C2), we find

$$A\left(\frac{d\Psi}{ds}\right)^3 + \frac{1}{2}[1 + O(\eta^{-1})](s - 1)A\frac{d\Psi}{ds}$$

$$+\eta^{-1/2}\left\{3\frac{dA}{ds}\left(\frac{d\Psi}{ds}\right)^2 + 3A\frac{d\Psi}{ds}\frac{d^2\Psi}{ds^2} + \frac{1}{2}[1 + O(\eta^{-1})]\left[(s - 1)\frac{dA}{ds} + A\right]\right\}$$

$$+\eta^{-1}\left\{3\frac{d^2A}{ds^2}\frac{d\Psi}{ds} + 3\frac{dA}{ds}\frac{d^2\Psi}{ds^2} + A\frac{d^3\Psi}{ds^3}\right\} + \eta^{-3/2}\frac{d^3A}{ds^3} \approx 0. \tag{C10}$$

This form of (C2) suggests expanding the amplitude function $A(s; \eta)$ as

$$A(s; \eta) = A_0(s) + \eta^{-1/2}A_1(s) + \cdots . \tag{C11}$$

The order unity balance of (C10) gives an equation for the function $\Psi(s)$:

$$\frac{d\Psi}{ds}\left[\left(\frac{d\Psi}{ds}\right)^2 - \frac{1 - s}{2}\right] = 0. \tag{C12}$$

We find that $d\Psi/ds$ either vanishes, in which case $\Psi(s)$ is constant, or we can have

$$\frac{d\Psi}{ds} = \pm\frac{1}{\sqrt{2}}(1 - s)^{1/2}, \tag{C13}$$

in which case (suppressing the integration constant in the amplitude)

$$\Psi = \mp\frac{\sqrt{2}}{3}(1 - s)^{3/2}, \tag{C14}$$

respectively. The solution corresponding to constant Ψ does not exhibit fast exponential variation; furthermore, the requisite leading-order approximation for $0 < s < 1$ must decay, rather than grow exponentially with decreasing s. Thus, only the positive-sign solution in (C14) is relevant.

From the order $\eta^{-1/2}$ balance of (C10), we find, using (C13),

$$(1 - s)\frac{dA_0}{ds} + \frac{1}{4}A_0 = 0, \tag{C15}$$

with solution

$$A_0 \propto (1 - s)^{1/4}. \tag{C16}$$

We have thus found a leading-order WKB approximation for $0 < s < 1$ in the form

$$\vartheta(s; \eta) \sim \Xi(\eta)(1 - s)^{1/4} \exp\left\{\eta^{1/2}\frac{\sqrt{2}}{3}(1 - s)^{3/2}\right\}, \tag{C17}$$

where $\Xi(\eta)$ is a prefactor. Matching with the inner approximation (46), we find

$$\Xi(\eta) = 4 \tan \frac{\pi}{8} \exp \left\{ -\eta^{1/2} \frac{\sqrt{2}}{3} \right\}. \tag{C18}$$

The WKB approximation (C17), which is now fully determined, is next matched with the free-end approximation (C7), using (C8a), to find

$$\xi(\eta) = \frac{2^{3/4} \pi^{1/2} 4 \tan \frac{\pi}{8}}{\sqrt{3}} \eta^{-1/12} e^{-\frac{\sqrt{2}}{3} \eta}. \tag{C19}$$

We then find from (C7), (C8b), and (C19) the leading-order exponential approximation (57) for $\vartheta(1; \eta)$ stated in the main text.

2. Shear flow

In the shear case, we have [cf. (50)]

$$\bar{u}(\eta) \sim \psi \eta^{-1/3} + \tilde{\psi} \eta^{-2/3} \quad \text{as} \quad \eta \to \infty, \tag{C20}$$

with $\psi = 2^{2/3}$ (Table II) and $\tilde{\psi} \doteq 0.693$ (Appendix B). The exponentially accurate differential equation (55) can therefore be written as

$$\frac{1}{\eta} \frac{d^3 \vartheta}{ds^3} - \frac{1}{2} [\psi \eta^{-1/3} + \tilde{\psi} \eta^{-2/3} + \cdots] (1-s) \frac{d\vartheta}{ds} + [\psi \eta^{-1/3} + \tilde{\psi} \eta^{-2/3} + \cdots] \vartheta \approx 0. \tag{C21}$$

A dominant-balance analysis of (C21) now suggests a free-end inner region of thickness order $1/\eta^{2/9}$. We accordingly define the strained arc length

$$\hat{\rho} = \eta^{2/9} (1-s), \tag{C22}$$

and expand

$$\vartheta(s; \hat{\rho}) = \hat{\Phi}(\hat{\rho}; \eta) + \cdots, \tag{C23}$$

holding $\hat{\rho} > 0$ fixed. From (C21), $\hat{\Phi}$ satisfies the differential equation

$$\frac{d^3 \hat{\Phi}}{d\hat{\rho}^3} - \frac{\psi}{2} \hat{\rho} \frac{d\hat{\Phi}}{d\hat{\rho}} - \psi \hat{\Phi} = 0, \tag{C24}$$

while (56) give the free-end boundary conditions

$$\frac{d\hat{\Phi}}{d\hat{\rho}} = 0, \tag{C25a}$$

$$\frac{d^2 \hat{\Phi}}{d\hat{\rho}^2} = 0 \quad \text{at} \quad \hat{\rho} = 0. \tag{C25b}$$

Up to a rescaling involving ψ, this is the same free-end problem as found in the uniform- and parabolic-flow cases [cf. (C5) and (C6)]. Indeed, the solution to (C24) and (C25) is

$$\hat{\Phi}(\hat{\rho}; \eta) = \hat{\xi}(\eta) \hat{\rho} I_{-2/3} \left(\frac{\sqrt{2\psi}}{3} \hat{\rho}^{3/2} \right), \tag{C26}$$

where the prefactor $\hat{\xi}(\eta)$ is to be determined [cf. (C7)].

Following the analysis in the uniform- and parabolic-flow case, we next derive a WKB approximation for $0 < s < 1$. Inspection of (C21) suggests the modified ansatz [cf. (C9)],

$$\vartheta(s; \eta) \propto A(s; \eta) \exp[\eta^{1/3} \Psi(s)], \tag{C27}$$

with the amplitude $A(s; \eta)$ expanded as

$$A(s; \eta) = A_0(s) + \eta^{-1/3} A_1(s) + \cdots. \tag{C28}$$

Substituting (C27), with (C28), into (C21), we find from a leading-order balance that the function $\Psi(s)$ satisfies

$$\frac{d\Psi}{ds}\left[\left(\frac{d\Psi}{ds}\right)^2 - \frac{\psi(1-s)}{2}\right] = 0, \tag{C29}$$

the relevant solution for matching being

$$\Psi(s) = \frac{\sqrt{2\psi}}{3}(1-s)^{3/2}, \tag{C30}$$

again the same as in the uniform- and parabolic-flow cases up to a rescaling [cf. (C14)]. A higher-order balance then shows that the amplitude $A(s)$ satisfies the differential equation

$$(1-s)\frac{dA_0}{ds} + A_0\left[\frac{1}{4} + \frac{\tilde{\psi}}{2\sqrt{2\psi}}(1-s)^{3/2}\right] = 0, \tag{C31}$$

which is essentially different from the corresponding (C15) in the uniform- and parabolic-flow cases owing to the dependence upon the constant $\tilde{\psi}$, representing the first algebraic correction to the flow. The solution to (C31) is

$$A_0(s) \propto (1-s)^{1/4}\exp\left\{\frac{\tilde{\psi}(1-s)^{3/2}}{3\sqrt{2\psi}}\right\}. \tag{C32}$$

We have thus found a leading-order WKB approximation for $0 < s < 1$ in the form

$$\vartheta(s;\eta) \sim \hat{\Xi}(\eta)(1-s)^{1/4}\exp\left\{\frac{\tilde{\psi}(1-s)^{3/2}}{3\sqrt{2\psi}}\right\}\exp\left\{\eta^{1/3}\frac{\sqrt{2\psi}}{3}(1-s)^{3/2}\right\}, \tag{C33}$$

where, by matching with the inner approximation (46), we find the prefactor as

$$\hat{\Xi}(\eta) = 4\tan\frac{\pi}{8} \times \exp\left\{-\frac{\tilde{\psi}}{3\sqrt{2\psi}}\right\}\exp\left\{-\eta^{1/3}\frac{\sqrt{2\psi}}{3}\right\}. \tag{C34}$$

It remains to match the WKB approximation (C33) with the free-end inner approximation (C26), which gives, using $\psi = 2^{2/3}$,

$$\hat{\xi}(\eta) = \frac{2^{11/12}\pi^{1/2}4\tan\frac{\pi}{8}}{3^{1/2}}\exp\left\{-\frac{\tilde{\psi}}{2^{5/6}3}\right\} \times \eta^{-1/18}\exp\left\{-\eta^{1/3}\frac{2^{5/6}}{3}\right\}. \tag{C35}$$

We then find from (C8b), (C26), and (C35) the leading-order exponential approximation (58) for $\vartheta(1;\eta)$ stated in the main text.

[1] E. Lauga, *The Fluid Dynamics of Cell Motility* (Cambridge University Press, Cambridge, UK, 2020), Vol. 62.

[2] S. Gsell, E. Loiseau, U. D'Ortona, A. Viallat, and J. Favier, Hydrodynamic model of directional ciliary-beat organization in human airways, Sci. Rep. **10**, 8405 (2020).

[3] O. H. Shapiro, V. I. Fernandez, M. Garren, J. S. Guasto, F. P. Debaillon-Vesque, E. Kramarsky-Winter, A. Vardi, and R. Stocker, Vortical ciliary flows actively enhance mass transport in reef corals, Proc. Natl. Acad. Sci. USA **111**, 13391 (2014).

[4] S. Nonaka, Y. Tanaka, Y. Okada, S. Takeda, A. Harada, Y. Kanai, M. Kido, and N. Hirokawa, Randomization of left–right asymmetry due to loss of nodal cilia generating leftward flow of extraembryonic fluid in mice lacking KIF3B motor protein, Cell **95**, 829 (1998).

[5] S. Nonaka, H. Shiratori, Y. Saijoh, and H. Hamada, Determination of left–right patterning of the mouse embryo by artificial nodal flow, Nature (London) **418**, 96 (2002).

[6] S. Nonaka, S. Yoshiba, D. Watanabe, S. Ikeuchi, T. Goto, W. F. Marshall, and H. Hamada, De novo formation of left–right asymmetry by posterior tilt of nodal cilia, PLoS Biol. **3**, e268 (2005).

[7] Y. Okada, S. Takeda, Y. Tanaka, J.-C. I. Belmonte, and N. Hirokawa, Mechanism of nodal flow: A conserved symmetry breaking event in left-right axis determination, Cell **121**, 633 (2005).

[8] S. Hanasoge, P. J. Hesketh, and A. Alexeev, Microfluidic pumping using artificial magnetic cilia, Microsyst. Nanoeng. **4**, 11 (2018).

[9] H. Gu, Q. Boehler, H. Cui, E. Secchi, G. Savorana, C. De Marco, S. Gervasoni, Q. Peyron, T.-Y. Huang, S. Pane *et al.*, Magnetic cilia carpets with programmable metachronal waves, Nat. Commun. **11**, 2637 (2020).

[10] W. Wang, Q. Liu, I. Tanasijevic, M. F. Reynolds, A. J. Cortese, M. Z. Miskin, M. C. Cao, D. A. Muller, A. C. Molnar, E. Lauga *et al.*, Cilia metasurfaces for electronically programmable microfluidic manipulation, Nature (London) **605**, 681 (2022).

[11] W. Gilpin, M. S. Bull, and M. Prakash, The multiscale physics of cilia and flagella, Nat. Rev. Phys. **2**, 74 (2020).

[12] A. Bausch and K. Kroy, A bottom-up approach to cell mechanics, Nat. Phys. **2**, 231 (2006).

[13] A. C. Callan-Jones and R. Voituriez, Actin flows in cell migration: From locomotion and polarity to trajectories, Curr. Opin. Cell Biol. **38**, 12 (2016).

[14] J. F. Marko and E. D. Siggia, Stretching DNA, Macromolecules **28**, 8759 (1995).

[15] T. T. Perkins, D. E. Smith, R. G. Larson, and S. Chu, Stretching of a single tethered polymer in a uniform flow, Science **268**, 83 (1995).

[16] Y.-N. Young, M. Downs, and C. R. Jacobs, Dynamics of the primary cilium in shear flow, Biophys. J. **103**, 629 (2012).

[17] M. D. Koch, C. Fei, N. S. Wingreen, J. W. Shaevitz, and Z. Gitai, Competitive binding of independent extension and retraction motors explains the quantitative dynamics of type IV pili, Proc. Natl. Acad. Sci. USA **118**, e2014926118 (2021).

[18] R. G. Cox, The motion of long slender bodies in a viscous fluid Part 1. General theory, J. Fluid Mech. **44**, 791 (1970).

[19] G. Batchelor, Slender-body theory for particles of arbitrary cross-section in Stokes flow, J. Fluid Mech. **44**, 419 (1970).

[20] J. Lighthill, Flagellar hydrodynamics, SIAM Rev. **18**, 161 (1976).

[21] J. B. Keller and S. I. Rubinow, Slender-body theory for slow viscous flow, J. Fluid Mech. **75**, 705 (1976).

[22] R. E. Johnson, An improved slender-body theory for Stokes flow, J. Fluid Mech. **99**, 411 (1980).

[23] I. Llopis, I. Pagonabarraga, M. Cosentino Lagomarsino, and C. P. Lowe, Sedimentation of pairs of hydrodynamically interacting semiflexible filaments, Phys. Rev. E **76**, 061901 (2007).

[24] B. Delmotte, E. Climent, and F. Plouraboué, A general formulation of bead models applied to flexible fibers and active filaments at low Reynolds number, J. Comput. Phys. **286**, 14 (2015).

[25] P. J. Żuk, A. M. Słowicka, M. L. Ekiel-Jeżewska, and H. A. Stone, Universal features of the shape of elastic fibres in shear flow, J. Fluid Mech. **914**, A31 (2021).

[26] Y. Liu, B. Chakrabarti, D. Saintillan, A. Lindner, and O. du Roure, Morphological transitions of elastic filaments in shear flow, Proc. Natl. Acad. Sci. USA **115**, 9438 (2018).

[27] O. Forgacs and S. Mason, Particle motions in sheared suspensions: IX. Spin and deformation of threadlike particles, J. Colloid Sci. **14**, 457 (1959).

[28] O. Forgacs and S. Mason, Particle motions in sheared suspensions: X. Orbits of flexible threadlike particles, J. Colloid Sci. **14**, 473 (1959).

[29] Y.-N. Young and M. J. Shelley, Stretch-Coil Transition and Transport of Fibers in Cellular Flows, Phys. Rev. Lett. **99**, 058303 (2007).

[30] V. Kantsler and R. E. Goldstein, Fluctuations, Dynamics, and the Stretch-Coil Transition of Single Actin Filaments in Extensional Flows, Phys. Rev. Lett. **108**, 038103 (2012).

[31] N. Quennouz, M. Shelley, O. du Roure, and A. Lindner, Transport and buckling dynamics of an elastic fibre in a viscous cellular flow, J. Fluid Mech. **769**, 387 (2015).

[32] A. M. Słowicka, N. Xue, P. Sznajder, J. K. Nunes, H. A. Stone, and M. L. Ekiel-Jeżewska, Buckling of elastic fibers in a shear flow, New J. Phys. **24**, 013013 (2022).

[33] N. Xue, J. K. Nunes, and H. A. Stone, Shear-induced migration of confined flexible fibers, Soft Matter **18**, 514 (2022).

[34] X. Xu and A. Nadim, Deformation and orientation of an elastic slender body sedimenting in a viscous liquid, Phys. Fluids **6**, 2889 (1994).

[35] L. Li, H. Manikantan, D. Saintillan, and S. E. Spagnolie, The sedimentation of flexible filaments, J. Fluid Mech. **735**, 705 (2013).

[36] B. Marchetti, V. Raspa, A. Lindner, O. du Roure, L. Bergougnoux, E. Guazzelli, and C. Duprat, Deformation of a flexible fiber settling in a quiescent viscous fluid, Phys. Rev. Fluids **3**, 104102 (2018).

[37] J. S. Wexler, P. H. Trinh, H. Berthet, N. Quennouz, O. du Roure, H. E. Huppert, A. Lindner, and H. A. Stone, Bending of elastic fibres in viscous flows: the influence of confinement, J. Fluid Mech. **720**, 517 (2013).

[38] L. Guglielmini, A. Kushwaha, E. S. G. Shaqfeh, and H. A. Stone, Buckling transitions of an elastic filament in a viscous stagnation point flow, Phys. Fluids **24**, 123601 (2012).

[39] S. A. Koehler and T. R. Powers, Twirling Elastica: Kinks, Viscous Drag, and Torsional Stress, Phys. Rev. Lett. **85**, 4827 (2000).

[40] B. Qian, T. R. Powers, and K. S. Breuer, Shape Transition and Propulsive Force of an Elastic Rod Rotating in a Viscous Fluid, Phys. Rev. Lett. **100**, 078101 (2008).

[41] A. Lamura, R. G. Winkler, and G. Gompper, Wall-anchored semiflexible polymer under large amplitude oscillatory shear flow, J. Chem. Phys. **154**, 224901 (2021).

[42] P. S. Doyle, B. Ladoux, and J.-L. Viovy, Dynamics of a Tethered Polymer in Shear Flow, Phys. Rev. Lett. **84**, 4769 (2000).

[43] T. Y. Lin, A. Saadat, A. Kushwaha, and E. S. G. Shaqfeh, Effect of length on the dynamics of wall tethered polymers in shear flow, Macromolecules **51**, 254 (2018).

[44] C. Pozrikidis, Shear flow over cylindrical rods attached to a substrate, J. Fluids Struct. **26**, 393 (2010).

[45] E. Wandersman, N. Quennouz, M. Fermigier, A. Lindner, and O. du Roure, Buckled in translation, Soft Matter **6**, 5715 (2010).

[46] Wolfram Research Inc., *Mathematica*, Version 13.1 (Wolfram Research Inc., Champaign, IL, 2022).

[47] S. Alben, M. Shelley, and J. Zhang, Drag reduction through self-similar bending of a flexible body, Nature (London) **420**, 479 (2002).

[48] M. Abramowitz and I. A. Stegun, *Handbook of Mathematical Functions with Formulas, Graphs, and Mathematical Tables* (U.S. Government Printing Office, Mineola, New York, 1964), Vol. 55.